Applied Physics A (2023) 129:467
https://doi.org/10.1007/s00339-023-06664-4

Applied Physics A
Materials Science & Processing

Influence of single and double interlayers on the electrical and current transport mechanism of Mo/*n*-Si Schottky diode and its microstructural and chemical properties

V. Manjunath[1,2] · B. Purusottam Reddy[1] · U. Chalapathi[1] · Boseong Son[1] · Huijin Kim[1] · Chang-Hoi Ahn[1] · Si-Hyun Park[1]

Received: 12 October 2022 / Accepted: 3 April 2023 / Published online: 6 June 2023
© The Author(s), under exclusive licence to Springer-Verlag GmbH, DE part of Springer Nature 2023

Abstract

This study examined the role of Si_3N_4 and ZrO_2 on the microstructural and electrical properties of Mo/n-Si Schottky diodes (SD) as single and double insulating layers between the Mo metal and Si semiconductor. Various characterization techniques and I–V measurements were used to analyze their optical, microstructural, chemical, morphological, and electrical properties at room temperature. The direct optical bandgaps of double interlayer films are higher than the single-layer films. XRD, FESEM, EDX, XPS, and AFM analysis revealed the Si_3N_4 and ZrO_2 films formation at the interface. The electrical properties of the Mo/n-Si (MS), Mo/Si_3N_4/n-Si (MIS), Mo/ZrO_2/n-Si (MIS) Schottky diodes (SD) are associated with the properties of the Mo/Si_3N_4/ZrO_2/n-Si (MIIS) Schottky diode (SD). In comparison to the MS Schottky diode (SD), the MIS and MIIS SDs demonstrate outstanding rectifying capability and low reverse leakage current. The MIIS SD achieves the highest barrier height (BH) than the MISs and MS SDs, which has led to the BH being adjusted by the insulating layers. Furthermore, the BH, n, and series resistance were analyzed using TE, Cheung's, Norde's, and the Chattopadhyay methods were similar, indicating consistency and validity. The current transport mechanism was investigated based on the forward-bias I–V plot. Finally, the reverse bias I–V performance of MS SD is controlled by Schottky emission mechanism. The MIS and MIIS SD were controlled by a Poole–Frenkel mechanism at lower regions and Schottky emission mechanism at higher regions. Thus, the MIIS double interlayer SD is appropriate for high-performance electrical and optoelectronic device applications.

Graphical abstract

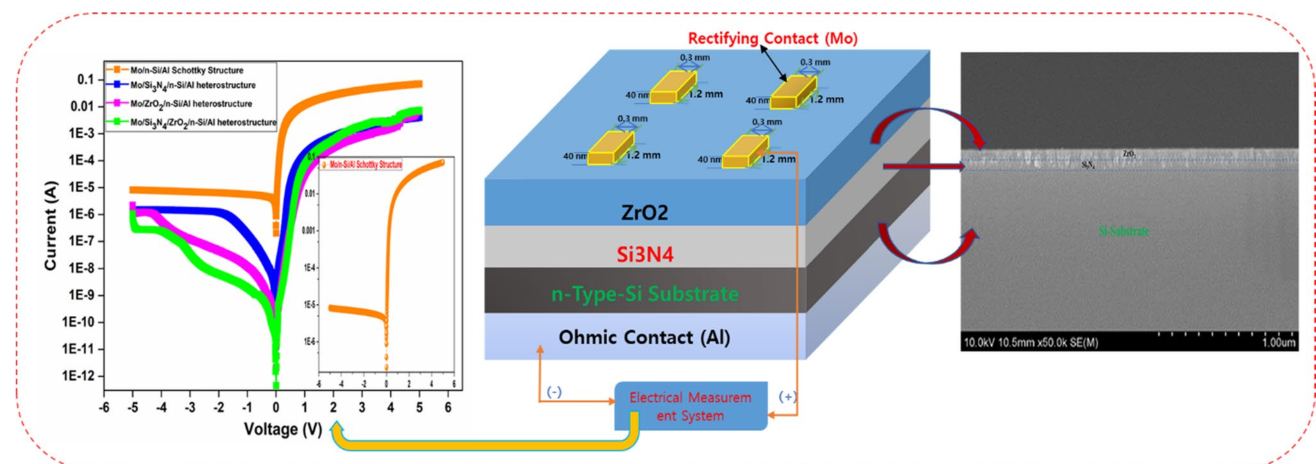

V. Manjunath and B. Purusottam Reddy have contributed equally.

Extended author information available on the last page of the article

Keywords 2D materials · Schottky diodes · Current transport mechanism · Optical bandgap · Chemical and microstructural properties

Abbreviations

TE	Thermionic emission
MS	Metal-semiconductor
MIS	Metal-insulator-semiconductor
MIM	Metal-insulator-metal
MIS	Metal-insulator-semiconductor
MIIS	Metal-insulator-insulator-semiconductor
XRD	X-ray diffraction
XPS	X-ray photoelectron spectroscopy
FESEM	Field emission scanning electron microscopy
AFM	Atomic force microscopy
EDX	Energy-dispersive X-ray spectroscopy
SBDs	Schottky barrier diodes
SD	Schottky diode
BH	Barrier height
n	Ideality factor

1 Introduction

Globally, accomplishing energy-efficient management in the commercialization of electronic devices for microelectronic and optoelectronic applications is challenging. Schottky barrier diodes (SBDs) such as metal-semiconductor (MS) and metal-insulator-semiconductor (MIS) diodes exhibit superior electrical properties when compared to other layered diodes such as P–N, Zener diodes, metal-insulator-metal (MIM), crystal diodes, tunnel diodes, and LEDs [1–3]. SBDs operated with a low forward bias level (0.2–0.3 V) can be employed in high frequency switching applications [4, 5]. MIS SBDs also play a vital role in various applications, including biological sensors, microelectronic devices, optical communication systems, and the generation of radio frequencies, owing to their excellent mechanical stability [6, 7]. An inorganic/organic insulating layer deposited in between a semiconductor substrate and a metal electrode would change the value of Schottky barrier height (SBH/Φ_b) at the formed junction [8]. Multiple methods have been employed to use a SiO_2 insulating layer at the interface of the metal-semiconductor diodes. According to previous literature, the SiO_2 insulating layer results in a significant leakage current. Therefore, alternative interfacial insulating layers to lower the leakage current of MIS diodes are essential [9]. High-*k* dielectric/two-dimensional (2D) materials such as TiO_2, MoO_3, SnO_2, HfO_2, ZrO_2, Si_3N_4, and In_2O_3 and with conventional metal electrodes (Au, Cu, Pt, Ti, Al, Mo, Sb, and Ni) attract considerable attention as interfacial layers and metal electrodes [10, 11]. The leakage currents of metal/ZrO_2, metal/HfO_2, metal/TiO_2, and metal/Si_3N_4 junctions on the semiconductor substrate have extremely low leakage currents compared to metal/SiO_2/semiconductor diodes. Furthermore, the use of high-*k* oxide layers increases the rate of rectification (RR = IF/IR)/shunt resistance [12–14]. Many previous studies have shown that high-*k* materials with higher dielectric constants can considerably improve the leakage current and carrier mobility of 2D semiconductors by minimizing Coulomb impurity scattering [15, 16].

ZrO_2 has been extensively investigated over the past decade owing to its suitable features, such as high thermal stability, high dielectric constant (20–25), wide bandgap (5.8–7.8 eV), ion-exchange capability [17], high ionic conductivity, low thermal conductivity, higher strength/melting point, and good chemical stability at the Zr/Si interface [18]. ZrO_2 material crystallizes into three phases at different temperatures: cubic (> 2370 °C), tetragonal (1170–2370 °C), and monoclinic (< 1170 °C). These characteristics make ZrO_2 an excellent material for use in solar cells [19], batteries [20], photocatalysis [21], fuel cells [22], gas sensors [23], heterojunctions [24], photonics [25], and electrochemical capacitors [26]. The improved device properties of high-electron-mobility transistors (HEMTs) utilizing in situ produced silicon nitride (Si_3N_4) have demonstrated prospects for use in a wide range of electronic devices [27–29]. Due to its outstanding dielectric strength ($\gtrsim 10^7$ V/cm), diffusion barrier, and high dielectric constant (~ 7.5), Si_3N_4 has been extensively investigated over the last decade. Si_3N_4 is also a good passivating dielectric for semiconductors such as Si and GaN with reduced surface densities [30]. The stoichiometry of Si_3N_4 is influenced by the deposition conditions employed [31]. Furthermore, because the insulating layer thickness influences the device performance, a thin insulating layer is necessary for good switching behavior [32, 33]. Therefore, investigating the characteristics of ultrathin interlayers (single/few layers) is challenging [1, 5, 16, 23, 24, 34–38, 66]. To reduce the interfacial defects in 2D devices, high dielectric constant and broad-bandgap materials are essential [16].

Because of their high specific surface area, atomically thin layers, single layers, or two-dimensional (2D) materials are attractive as channel materials for electronic and optoelectronic device applications [16]. Further, investigating the interaction of 2D materials with semiconductor substrates at interfaces with functional oxides and multifunctional devices with novel properties via coupling is important.

These findings can provide insights for innovative 2D device modulation via functional oxide interface engineering. The current study focuses on the development of Mo/Si_3N_4/n-Si and Mo/ZrO_2/n-Si (metal-insulator-semiconductor; MIS) single layers and Mo/Si_3N_4/ZrO_2/n-Si (metal-insulator-insulator-semiconductor; MIIS) double interlayer SDs. In addition, to increase the performance and stability of the devices, the researchers used high-work function metals to prepare Schottky devices. The work function values of Pt, Au, Cr, Ag, Mo, and W, are 5.65, 5.1, 4.5, 4.26, 4.6, and 4.55 eV, respectively. Molybdenum (Mo) metal is used as a Schottky metal in this work; Mo metal gave the ReRAM properties with good work function (4.6 eV) [39]. The metals Au and Pt are very expensive and have a much higher work function value. And which is a standard electrode material with excellent electrical properties. So, the rectangular Mo metal electrodes were deposited on an n-Si substrate, and MIS/MIIS was compared with the MS diode. The optical, microstructural, chemical, and surface morphological characteristics of Si_3N_4, ZrO_2, and Si_3N_4/ZrO_2 films were examined. Finally, current–voltage (I–V) characteristics at room temperature were used to examine the electrical characteristics of the Mo/Si_3N_4/ZrO_2/n-Si (MIIS) SD. The results of Mo/Si_3N_4/n-Si, Mo/ZrO_2/n-Si (MIS) SDs, and MS SDs could be correlated with the MIIS SDresults.

This study's major objective is to investigate into how the Mo/n-Si SD's electrical properties are affected by the (Si_3N_4/ZrO_2) double interlayer.For this purpose, (Si_3N_4 and ZrO_2) were fabricated by the sputtering method and both their electrical, optical, microstructural chemical properties were investigated by UV–Vis-NIR spectrophotometry, grazing index X-ray diffraction (GIXRD), field emission scanning electron microscopy (FESEM), energy-dispersive X-ray spectroscopy (EDX), X-ray photoelectron spectroscopy (XPS), and atomic force microscopy (AFM) were used to analyze the optical properties. Following that, their n, BH, and R_S values were determined and compared using the TE emission, Cheung's, Norde's, and SP-V techniques. These findings demonstrate that compared to the individual Si_3N_4 and ZrO_2 single interlayer and without interlayered Mo/n-Si SDs, the (Si_3N_4/ZrO_2) double interlayer leads to an increase in BH and a decrease in n and R_S resultant values.

2 Experimental and characterizations techniques

In this study, 1 cm × 1 cm Si sample pieces from an 8″ Si (100) wafer with a thickness of 600 µm was used. To develop n-Si-based SDs, Si_3N_4 and ZrO_2 interlayers were used. The RAC technique was used on a regular clean n-Si wafer with a resistivity of 1–10 Ω cm prior to deposition [40]. A HF: H_2O (1:8) solution was used to remove native oxides, followed by rinsing in deionized water. To obtain a satisfactory ohmic contact, thermal evaporation was used to generate an Al metallization of 45 nm thickness on the back (rough) side of the cleaned substrate (Si), which was annealed at 300 °C for 5 min in N_2 gas using a rapid thermal processing furnace. Thereafter, RF-magnetron sputtering was used to deposit Si_3N_4 and ZrO_2 thin films on the n-Si (smooth side) and quartz glass substrates. Si_3N_4/Si diodes (three samples) were prepared using a 50 mm diameter Si_3N_4 target (99.9% purity) in ambient air of argon as the sputter gas. ZrO_2/Si (three samples), and Si_3N_4:ZrO_2/Si (three samples) diodes were also prepared under the same deposition conditions. To remove surface contamination, the target was pre-sputtered for 10 min in an Ar gas environment. Finally, using direct current sputtering equipment, Mo was deposited as a top metal electrode with a thickness of 40 nm in a rectangular area of 1.2 mm × 0.3 mm under the conditions listed in Table 1. The Mo/Si_3N_4/Si, Mo/ZrO_2/Si, and Mo/Si_3N_4/ZrO_2/Si SDs are shown schematically in Fig. 1a, b, respectively. To compare the electrical characteristics, interlayered SDs (MIS) without interlayered SDs (MS) were developed under identical conditions. UV–Vis-NIR spectrophotometry, GIXRD, FESEM, EDX, XPS, and AFM were used to analyze the optical, microstructural, elemental, morphological properties, and chemical composition of the prepared Si_3N_4/

Table 1 Deposition parameters of Si_3N_4, ZrO_2 thin films, and Molybdenum metal electrode

Parameter	RF magnetron sputtering (optimized values)	RF magnetron sputtering (optimized values)	DC magnetron sputtering (optimized values)
Sputter target	ZrO_2	Si_3N_4	Mo
Target size and purity	2-inch with 99.99% purity		
Base pressure	3×10^{-6} Torr		
Working pressure	5.2×10^{-3} Torr	5.5×10^{-3} Torr	5.7×10^{-3} Torr
RF power	110 W	90 W	70 W
Substrate to target distance	70 mm	70 mm	70 mm
Argon partial pressure	8×10^{-5}–5×10^{-4} Torr	7×10^{-5}–5×10^{-4} Torr	6×10^{-5}–5×10^{-4} Torr
Film thickness	50 nm	40 nm	40 nm

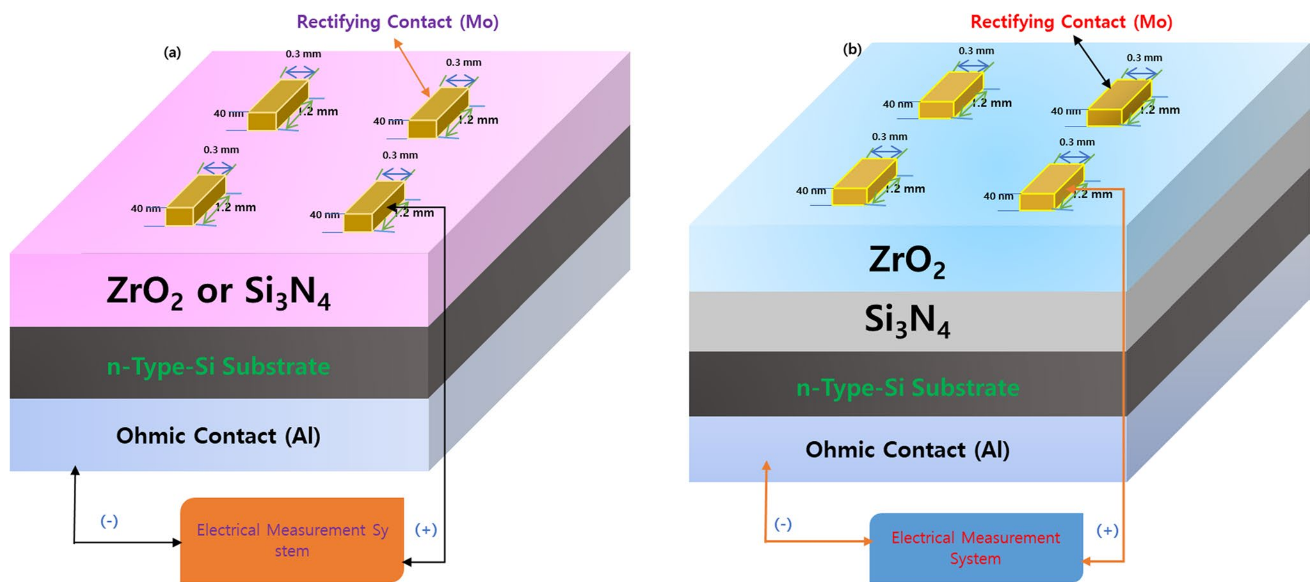

Fig. 1 Schematic configuration of the fabricated Mo/Si_3N_4/n-Si, Mo/ZrO_2/n-Si (MIS), Mo/Si_3N_4/ZrO_2/n-Si (MIIS) (single layer and double layer) SDs

Si, ZrO_2/Si, and Si_3N_4/ZrO_2/Si devices. Finally, the electrical characteristics of the Mo/n-Si (MS) SD and Mo/Si_3N_4/Si, Mo/ZrO_2/Si (MIS), and Mo/Si_3N_4/ZrO_2/Si (MIIS) (single/double interlayer) SDs were investigated at room temperature using a Keithley source meter (2636).

3 Results and discussion

3.1 Evaluation of optical, microstructural, surface morphology, chemical, and electrical properties

3.1.1 Optical absorption study

UV–Vis-NIR spectroscopy was used to analyze the electronic structures of the Si_3N_4, ZrO_2, and Si_3N_4:ZrO_2 films at ambient temperature. Absorption was caused by the electronic transitions inside the Si_3N_4 and ZrO_2 materials. Figure 2 shows the UV–Vis spectra of the single layer and double interlayer coatings on quartz. The double interlayer film displayed a color shift from blue to violet compared to the single-layer films. The highest absorbance for the double interlayer film was obtained at approximately 266 nm, with a peak at 209 nm, as shown in Fig. 2c. Furthermore, beyond 280 nm, the absorbance remained constant up to 1000 nm. The double interlayer shifts the values of absorption to a greater wavelength range than the single layer because of the deep black pigmentation of the films, roughness of the surface, and increase in grain boundaries, in addition to the stimulation or transfer of charge carriers (Fig. 2a) [41, 42]. Tauc's plot was used to determine the direct optical bandgap (E_g) in the single and double interlayer films, as shown in Fig. 2b, c. The resulting Tauc plot can be used to estimate the direct E_g by extrapolating the $(\alpha h\nu)^2$ vs. '$h\nu$' curve below zero absorbance [43]

$$\alpha h\nu = E_D\left(h\nu - E_g\right)^{1/2}, \tag{1}$$

where E_D is a constant, $h\nu$ is the photon energy, and α is the absorbance coefficient.

The E_g values of bulk Si_3N_4 and ZrO_2 were 5.3 and 4.9 eV, respectively. The single and double interlayer films had direct bandgap energies of 5.20, 4.31, and 3.90 eV, respectively. These results agree with those of previous studies [44, 45]. Because of the increased Fermi energy level, single-layered films have a larger bandgap than double-layered films. This could be due to the production of O_2 vacancies in the Si_3N_4, and ZrO_2 sites and crystalline formation, which minimized defects [46]. These findings affect the electrical transitions between the VB and CB (valence and conduction bands), which reduces the energy values of the Si_3N_4:ZrO_2 film. An uncoated quartz substrate was used as the baseline correction reference for optical absorption.

3.1.2 X-ray diffraction study

The grazing incidence x-ray diffraction (GIXRD) scans of the Si_3N_4, ZrO_2, and Si_3N_4:ZrO_2 films on Si are shown in Fig. 3. Si_3N_4 showed a significant intensity reflection of the (3 2 0) and (1 0 4) planes of α-Si_3N_4 at 2θ values of 34.46° and 59.26°, respectively, indicating the existence

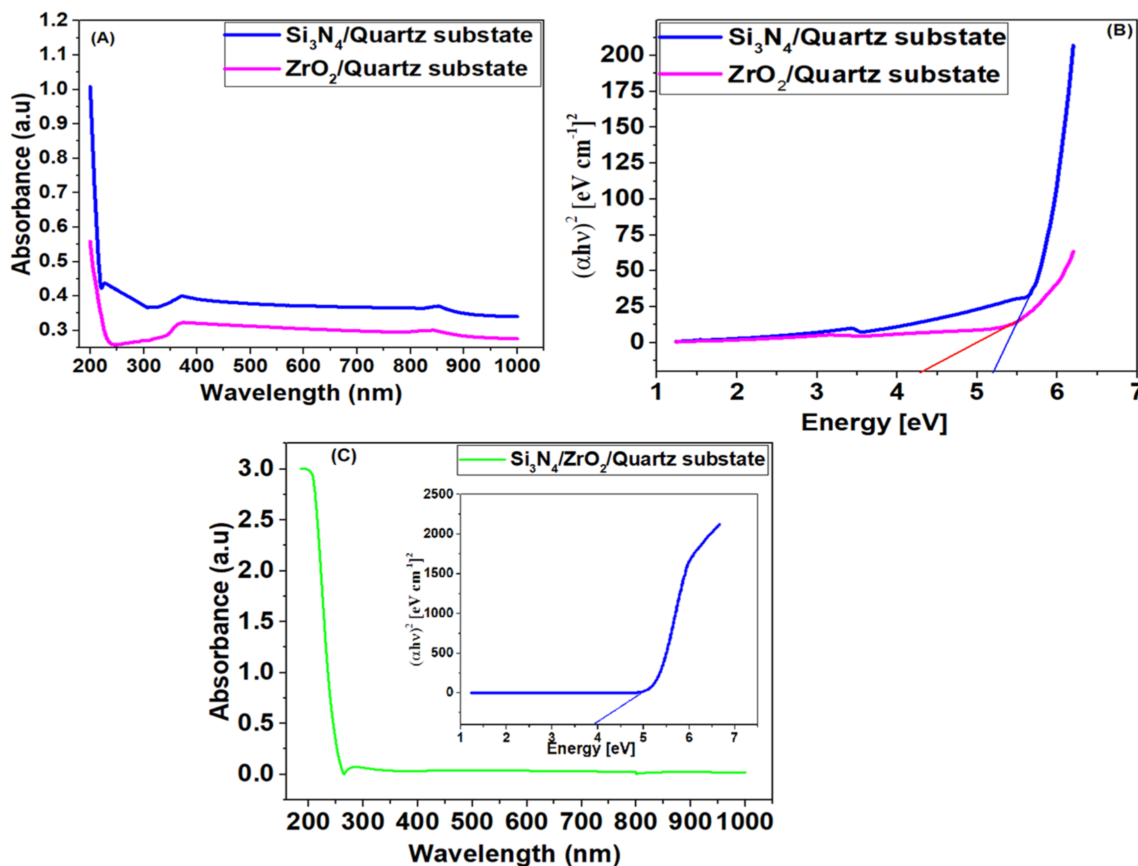

Fig. 2 **a** Absorbance-wavelength spectrum, **b** Tauc's plot: $(\alpha h\nu)^2$-hν for Mo/Si_3N_4/n-Si, Mo/ZrO_2/n-Si(MIS) SDs, and **c** absorbance-wavelength spectrum and Tauc's plot: $(\alpha h\nu)^2$-hν for Mo/Si_3N_4/ZrO_2/n-Si (MIIS) SD

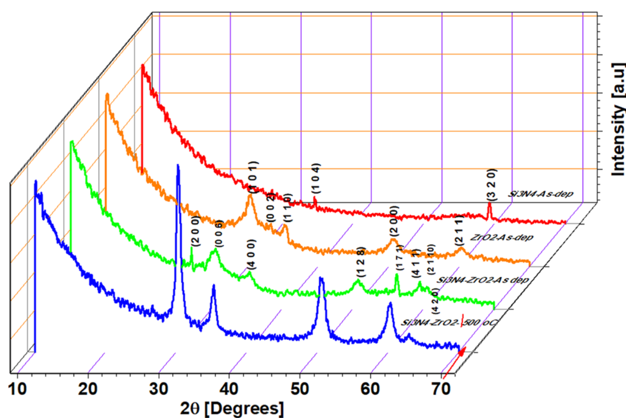

Fig. 3 XRD spectrum for **a** Si_3N_4, **b** ZrO_2, and **c**, **d** Si_3N_4/ZrO_2 films on Si substrate

of hexagonal instead of amorphous [36, 38] (Fig. 3a). The high-intensity refractions of ZrO_2 (1 0 1), $ZrO_{1.99}$ (0 0 2), ZrO_2 (1 1 0), and ZrO_2 (2 1 1) planes are shown in Fig. 3b at 2θ values of 30.55°, 33.37°, 35.30°, 50.56°, and 60.26° confirming the predominant tetragonal phase. Figure 3c, d show the as-deposited and annealed XRD plot of Si_3N_4:ZrO_2 thin films on n-Si, respectively. Figure 3c shows the high-intensity refractions of the $ZrSiO_4$ (2 0 0), $Zr_7O_{11}N_2$ (0 0 6), Zr_2ON_2 (4 0 0), $Zr_7O_{11}N_2$ (1 2 8), $ZrSi_2$(1 7 1), $ZrSiO_4$ (4 1 1), and $Zr_7O_{11}N_2$ (2 1 10) planes at 2θ values of 27.11°, 30.51°, 35.36°, 50.76°, 56.18°, 59.43°, and 60.48°, respectively. We observed new phases owing to the combination of two layers, which proved the existence of tetragonal rather than rhombohedral or orthogonal phases. Figure 3d shows the Si_3N_4:ZrO_2 thin film at 500 °C for 10 min in an N_2 atmosphere to verify its crystallinity. Compared with the as-deposited films, the intensity of the annealed film increased. This indicates that the Si_3N_4:ZrO_2 interface formed an interfacial phase after annealing. XRD results revealed that the single layer and double interlayer films deposited on n-Si had a significant impact on the electrical characteristics of both SDs [47, 48].

3.1.3 Surface morphology study

As shown in Fig. 4a–c, XPS analysis was used to investigate the surface elemental and bonding states of the prepared

Si_3N_4, ZrO_2, and Si_3N_4:ZrO_2 films on the Si substrate using single chromatic Al Kα radiation (1486.6 eV). To calibrate all the peaks, we used the C 1s peak, which has a binding energy of 284.5 eV. In Fig. 4a, the significant peaks of the survey spectrum correlate with the N, Si, and O in the film. The presence of Si–N bonds can be observed in the narrow-scan XPS spectra of Si 2p and N 1s (insets of Fig. 4a). This is because the main peak in the Si 2p spectrum centered at 101.7 eV is assigned to the Si–N bonds. The dominant peak in the N 1s spectrum centered at 398 eV is due to the N–Si bonds [49]. The core-level Zr 3d spectrum reveals two spin–orbit elements with an energy split of 2.4 eV, the Zr $3d_{5/2}$ peak with a binding energy of 183.36 eV verifies that the oxidation state is Zr^{4+} [30], and the peak of Zr $3d_{3/2}$ is positioned at 185.67 eV, as shown in the insets of Fig. 4b. The prominent peak at 530.6 eV in the O 1s spectra is attributed to the Zr–O bond in ZrO_2 [34]. Further, Fig. 4c shows the XPS survey spectrum and elemental splitting of the Si_3N_4:ZrO_2 (double interlayer) films. The presence of Si, Zr, N, and O was observed. The small peaks in Fig. 4a–c are attributed to C, Ar, and O. Ar peaks appeared because of surface cleaning prior to the XPS measurements. However, the C and O peaks originate may be due to the residual surface contamination and/or residual atmospheric gases in the sputtering chamber [35, 50].

3.1.4 SEM–EDX analysis

SEM was used to investigate the morphology of the Si_3N_4, ZrO_2, and Si_3N_4:ZrO_2 (single and double interlayer) films (Fig. 5a, c, e). A homogeneous surface with small equiaxed grains is observed on all films, indicating that the RF-magnetron sputtered single and double interlayer films are uniform, densely packed, accurate on the surface, and exhibit island growth. The EDX spectra of the single-and double interlayer films indicate the existence of N, O, and Si in (Fig. 5b), Zr, O, and Si in (Fig. 5d), and Zr, Si, N, and O in (Fig. 5f). The thicknesses of the deposited films were determined using cross-section SEM. Even though we deposited two layers on the substrate, the Si_3N_4:ZrO_2 layer thickness

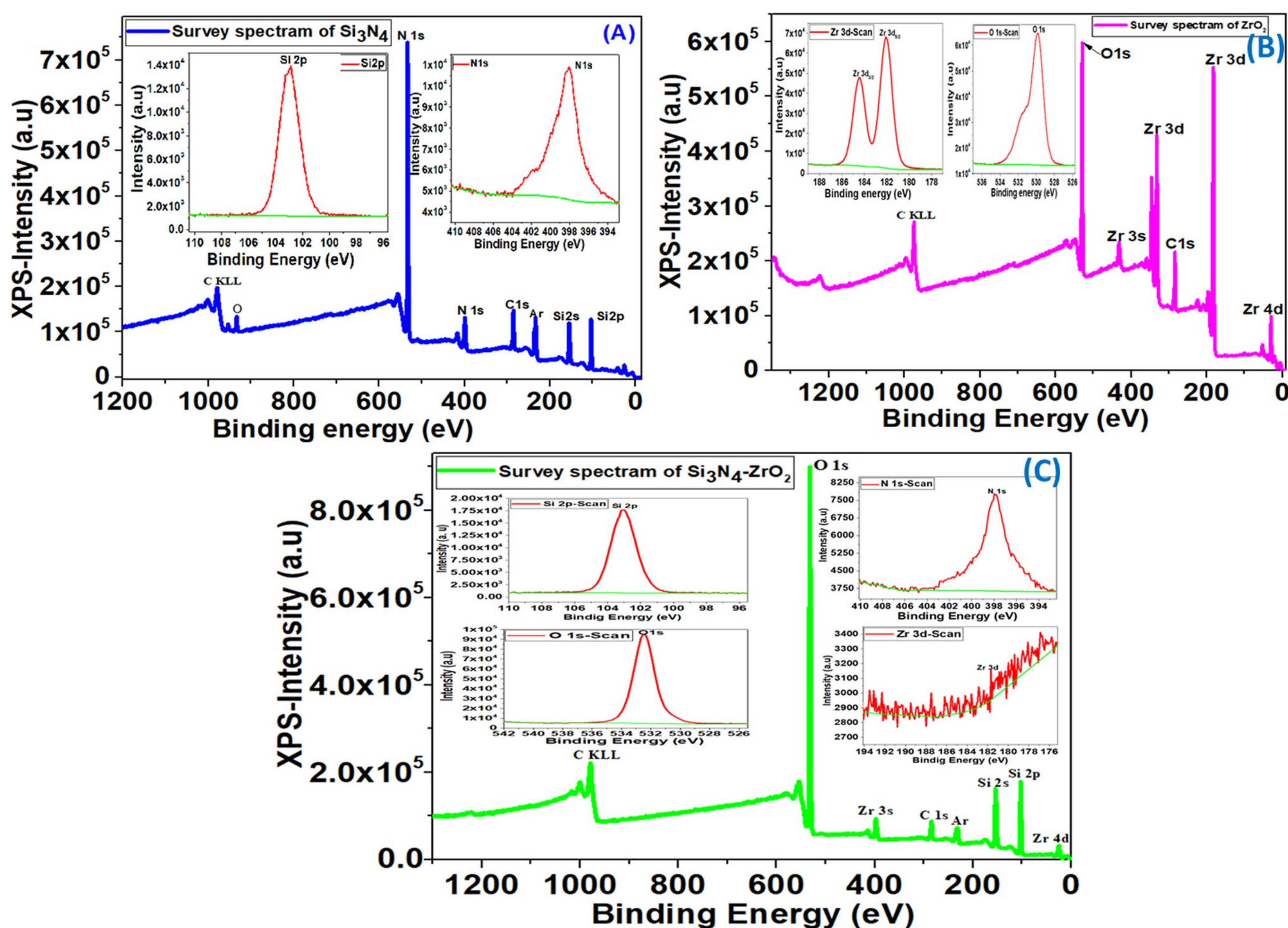

Fig. 4 **a–c** A typical survey scan XPS spectrum of the samples, the insets show the narrow-scan XPS spectra of the **a** Si 2p and N 1s: **b** Zr $3d_{5/2}$, Zr $3d_{3/2}$, and O 1s: **c** Si 2p, N 1s, O 1s, and Zr 3d energy level

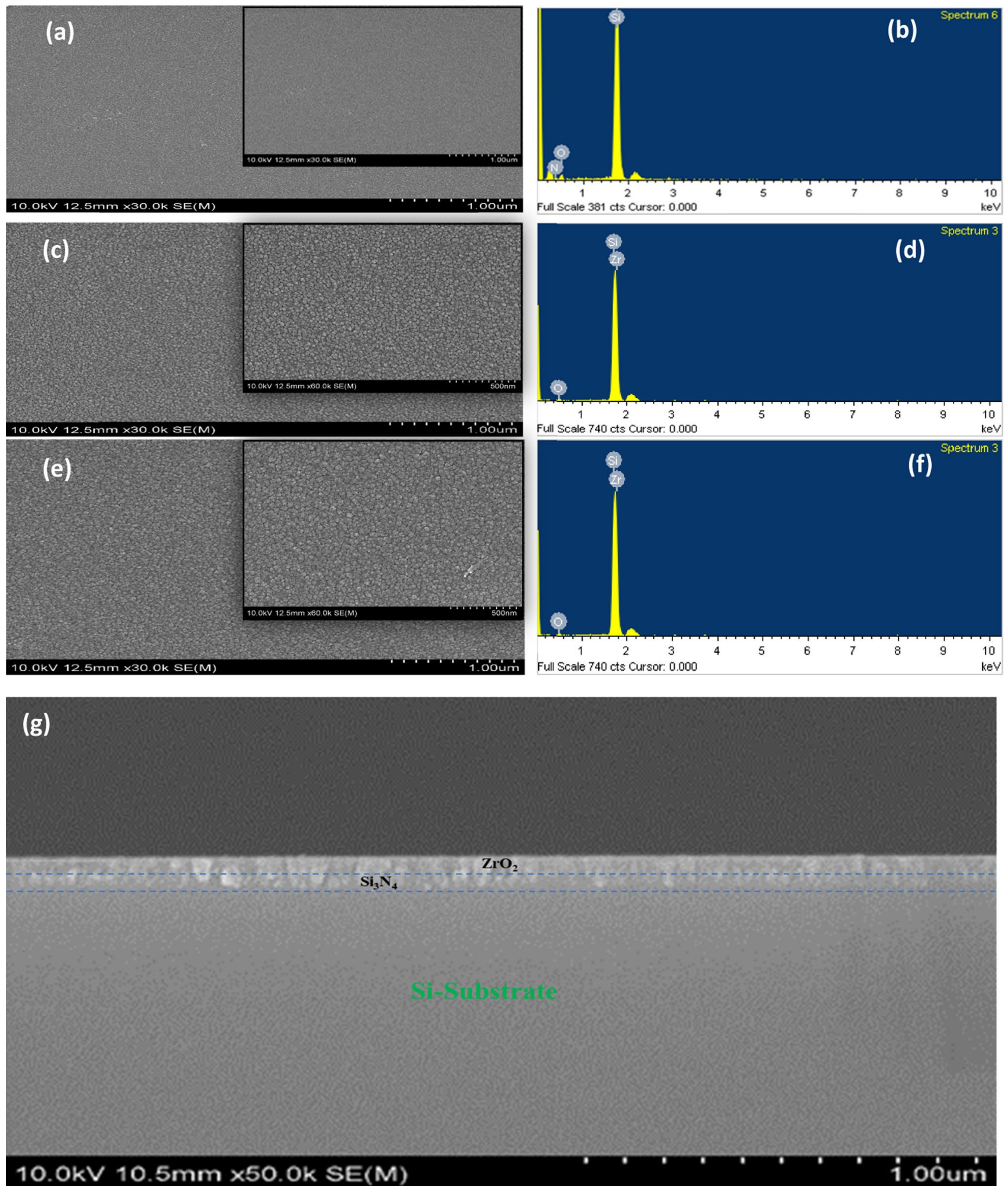

Fig. 5 SEM images and EDX spectrum of **a**, **b** for Si_3N_4, **c**, **d** for ZrO_2, **e**, **f**, **g** for Si_3N_4/ZrO_2 films on Si substrate

was 80–100 nm. Figure 5g shows the cross-section of the double interlayer film. The grain size of the double interlayer film was larger than that of the single layer. The XRD, XPS, SEM, and EDX results confirmed the formation of Si_3N_4:ZrO_2 uniform thin films on an n-Si substrate using sputtering, and the results are presented in Table 2.

3.1.5 AFM analysis

Using AFM measurements, we studied the surface topography of the Si_3N_4 and ZrO_2 films. And the 2D and three-dimensional (3D) topographic pictures from AFM, and the related surface roughness histogram (area = 3 μm × 3 μm) of the Si_3N_4, and ZrO_2 single layer s, and Si_3N_4:ZrO_2 double interlayer on n-Si, are shown in Fig. 6a–i. AFM 2D-pictures2D pictures spherical-shaped grains that are homogeneous, continuous, and dense (Fig. 6a, d, g). The 3D images in Fig. 6c, f, i show a combination of the microscopic particles in establishing a homogeneous distribution on the n-Si substrate. From Fig. 6b, e, h, the (R_a) average roughness and root mean square (RMS) of Si_3N_4, and ZrO_2 single layers and Si_3N_4:ZrO_2 double interlayer on n-Si was 0.67, 1.25, and 1.32 nm, and 0.875, 1.589, and 1.662, respectively. The surface topology of the prepared films is significantly influenced by the double interlayer [51, 52]. The film thickness was projected to increase when two insulating layers were added, resulting in improved electrical characteristics of the films. Consequently, the topological results were consistent with the XRD, XPS, and FESEM analyses.

3.2 Evaluation of electrical characteristics of MS diode, MIS, and MIIS SDs

3.2.1 I–V characteristics of MS diode, MIS, and MIIS SD

To correlate the structural investigations of Si_3N_4 and ZrO_2 with the electrical characteristics, we prepared Mo/Si_3N_4/n-Si, Mo/ZrO_2/n-Si MIS (single layer), Mo/Si_3N_4/ZrO_2/n-Si MIIS (double interlayer) SDs, and a Mo/n-Si as the standard MS SD as shown in Fig. 7; Fig. 1 shows the schematic structure of these SDs. The prepared Mo/Si_3N_4/ZrO_2/n-Si SDs exhibited good rectifying behavior. For the applied forward/reverse bias voltage, the current through the MIIS SD was significantly lower than that of the MIS and standard MS diodes. Figure 7 depicts the usual current–voltage (I–V) properties of the MS, MIS, and MIIS SDs. Compared with the MS diode, both the single (MIS) and double (MIIS) interlayer SDs demonstrated superior rectification. Compared to the Mo/n-Si diode (6.57×10^{-6} A at − 1 V), the reverse current leakages recorded in the Mo/Si_3N_4/n-Si (1.83×10^{-7} A at − 1 V) and Mo/ZrO_2/n-Si SDs (1.21×10^{-8} A at − 1 V) were much lower. Compared to the SD and single layered SDs, the reverse current leakage of the Mo/Si_3N_4/ZrO_2/n-Si SD (1.95×10^{-9} A at − 1 V) is significantly lower, which could be due to the potential barrier estimated by selecting insulating layers between the metal (Mo) and semiconductor (n-Si). Furthermore, thermionic emission (TE) theory was used to evaluate the I–V characteristics, the current through the SD with the effect of *RS* and an interlayer at forward bias ($V > 3kT/q$) is determined by the following relationship [53].

$$I = I_0 \exp\left[\frac{q\left(V - IR_s\right)}{nkT}\right]\left\{1 - \exp\left[\frac{q\left(V - IR_S\right)}{kT}\right]\right\} \quad (2)$$

where IR_S, V, T, q, k, n, and I_0, A, A^*, and Φ_b has conventional meanings [1, 2]. The reverse saturation current (I_0) is obtained from the intercept of the plot of ln I versus V at V = 0, given by

$$I_0 = AA^*T^2 \exp\left(-\frac{q\Phi_b}{kT}\right) \quad (3)$$

After determining the saturation current I_0, the Φ_b can be calculated using the expression

$$\Phi_b = \frac{kT}{q}\ln\left(\frac{AA^*T^2}{I_0}\right) \quad (4)$$

The ideality factor (n) values measures the diode's conformity to pure TE, it is determined using the relationship from the slope of the linear region of forward bias ln I–V.

$$n = \frac{q}{kT}\left(\frac{dV}{d(\ln I)}\right) \quad (5)$$

The on/off ratio, barrier height (BH), ideality factor (n) of the Mo/n-Si SD are 10^2, 0.71 eV, 1.23, respectively, whereas those of Mo/Si_3N_4/n-Si and Mo/ZrO_2/n-Si SDs are 10^5, 0.88 eV, 1.65, and 10^5, 0.99 eV, 1.31, respectively. Compared to the MS diode and MIS (single layer) SDs, the on/off ratio, BH, and n of the Mo/Si_3N_4/ZrO_2/n-Si (double

Table 2 Elemental ratio analyses for the Si_3N_4, ZrO_2, and Si_3N_4:ZrO_2 films on Si substrate

Element	Weight%	Atomic%
Si_3N_4 thin film		
N	8.01	2.30
O	7.06	10.92
Si	84.93	86.78
Total	100	
ZrO_2 thin film		
O	6.14	11.05
Si	83.56	85.70
Zr	10.30	3.25
Total	100	
Si_3N_4:ZrO_2 thin films		
N	2.20	1.25
O	11.06	15.92
Si	79.53	82.73
Zr	7.21	2.10
Total	100	

Fig. 6 **a**, **d**, **g** 2D surface morphology. **b**, **e**, **h** height profiles of 2D surface morphology, **c**, **f**, **i** 3D surface morphology of Si_3N_4, ZrO_2, and Si_3N_4/ZrO_2 films on Si substrate through AFM

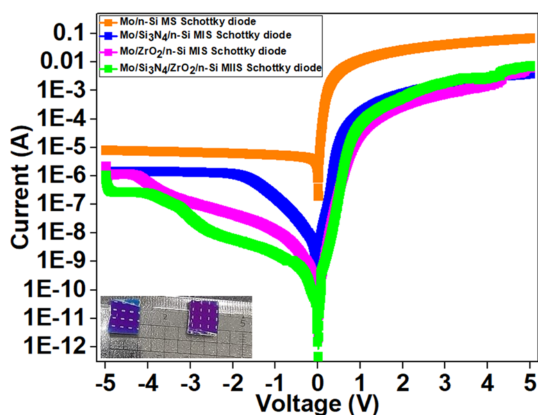

Fig. 7 Typical I–V characteristics of the fabricated Mo/n-Si (MS) SD, Mo/Si_3N_4/n-Si, Mo/ZrO_2/n-Si (MIS), $Mo/Si_3N_4/ZrO_2$/n-Si (MIIS) (single layer and double layer) SDs

interlayer) SD increased to 10^6, 1.04 eV, and 1.75, respectively. The successful reduction of n-type defect growth through the deposition of the insulator layer in the MIIS SD is attributed to the increased BH values [54, 55, 65]. Furthermore, negative charges are more prevalent in MIIS and MIS SDs than in MS diodes, which can be ascertained to the electron traps formed at the Si junction and then strongly associated with Si vacancies formed closer to the substrate surface during double-interlayer deposition [56].

3.2.2 Cheung's mechanism of MS diode and MIS SDs

Determining BH, and n from the nonlinear region of the I–V graph is not accurate. Therefore, Cheung mechanisms are used to calculate the BH, n, and series resistance (R_S) from the nonlinear region of the forward basic I–V graph, similar to the mechanism utilized in our earlier study [48]. Figure 8a–c show the graphs of dV/d(lnI)–I

and H(I)–I for the MS SD, the MIS single layer, and MIIS double interlayer SDs, respectively. The slope of the plot of dV/d(lnI)–I is R_S, and the y-axis intercept is nkT/q, which is associated with the n values. Using the n values obtained from the dV/d(lnI)–I graph, R_S and BH are calculated using the slope and y-axis ordinate via linear curve fitting. From the dV/d(lnI)–I graph, the R_S and n values of the MS diode are 64 Ω and 1.16, respectively. The BH and R_S values for the MS diode are 0.72 eV and 63 Ω from the H(I)–I graph (Fig. 8a). The R_S and n values for Mo/Si_3N_4/n-Si, Mo/ZrO_2/n-Si, and Mo/Si_3N_4/ZrO_2/n-Si SDs have been calculated to be 3946 and 1.75, 7711 Ω and 1.65, and 3602 Ω and 1.28, respectively, from the dV/d(lnI)–I graph (Fig. 8b). The values of BH and R_S obtained from the H(I)–I plot in Fig. 8c for the Mo/Si_3N_4/n-Si, Mo/ZrO_2/n-Si, and Mo/Si_3N_4/ZrO_2/n-Si SDs are 0.82 eV and 4193 Ω, and 1.00 eV and 7271 Ω, and 1.12 eV and 2675 Ω, respectively. The I–V technique agreed well with the BH values calculated using Cheung's method. Furthermore, the values of R_S calculated from the dV/d(lnI)–I graph are identical to the values calculated from the H(I)–I graph, demonstrating that Cheung's method is accurate. Furthermore, the values of R_S of the MIS and MIIS SDs are larger than those of the MS diode. This discrepancy implies a decrease in the rapidly increased rate of the current induced by the injection of space charge into the Si_3N_4 and ZrO_2 insulating layers at a higher voltage. Furthermore, compared to the values obtained using the I–V technique, the values of ideality factors calculated using Cheung's functions are higher. This demonstrates the presence of effects like R_S and BH according to the voltage drop across the interface states and the interface layer with applied bias in the low region of voltage in the (I–V) graph [57, 66, 67].

3.2.3 Norde's technique of MS diode and MIS SDs

Further, the R_S and BH of the MS SD, MIS, and MIIS SDs were calculated from the techniques described by Norde (Fig. 9a) [58], which were also used in our earlier study [16]. The BH and R_S values for Mo/n-Si diode, Mo/Si_3N_4/n-Si, Mo/ZrO_2/n-Si, and Mo/Si_3N_4/ZrO_2/n-Si SDs are 0.73 eV and 94 Ω, 0.89 eV and 159 k Ω, 1.02 eV and 2096 k Ω, and 1.16 eV and 53 M Ω, respectively. The values of BH calculated using Norde's method were larger than those calculated using the FB I–V plot, which could be attributed to the deviations from the ideal TE caused by the presence of an interlayer at the interface. Norde's technique may not be appropriate for rectifying junctions with a high ideality factor. Consequently [16, 69], the BH, and R_S values evaluated using Norde's technique are higher than all the calculated from Cheung functions, which could be owing to Norde's plot resultant values calculated from a full part of the FB I–V data of SDs.

3.2.4 Chattopadhyay mechanism of MS diode, MIS, and MIIS SDs

A negative oxide layer forms on the semiconductor surface when the metal and semiconductor come into direct contact [59]. The BH values can be calculated using the critical surface potential Ψ_{SP} (I_C, V_C), where V_C is the critical voltage, and n = 1/α as the experimental value [46, 48, 60]. Further, Ψ_{SP} value can be determined using an equation and a process utilized in our previous study [8]. For the MS SD, MIS, and MIIS SDs, the calculated BH, 'n' values are 0.71 eV, 0.92 eV, 0.91 eV, and 0.98 eV for BH, and 1.19, 1.81, 1.57, and 1.45 for n, as shown in Fig. 9b. The FB I–V, Cheung's, Norde's, and Ψ_{SP}-V methods yielded almost identical BH

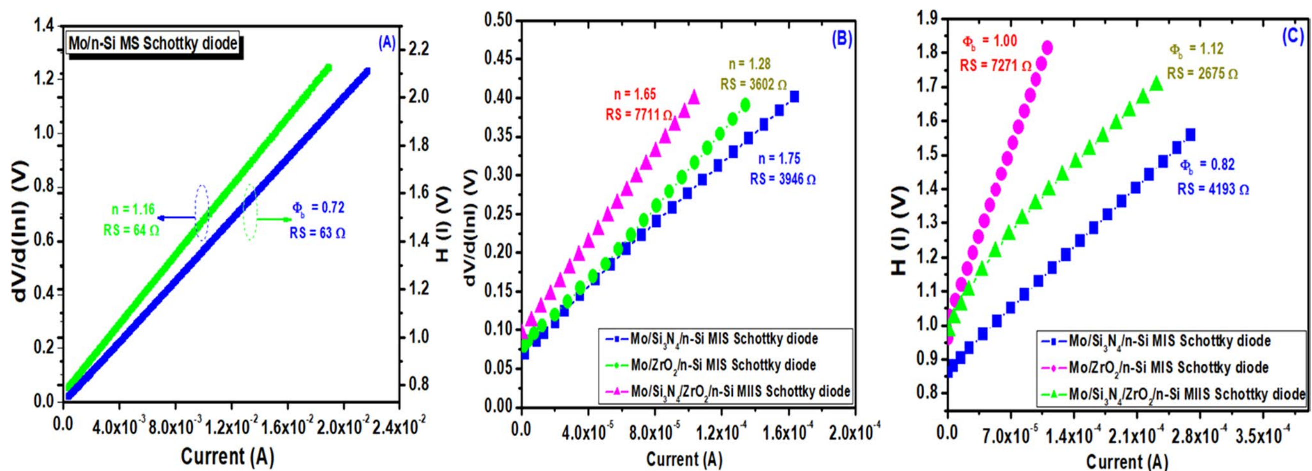

Fig. 8 **a** dV/d(lnI)–I, and H(I)–I plots for the Mo/n-Si (MS) SD, **b**, **c** for the Mo/Si_3N_4/n-Si, Mo/ZrO_2/n-Si(MIS), Mo/Si_3N_4/ZrO_2/n-Si (MIIS) (single layer and double layer) SDs

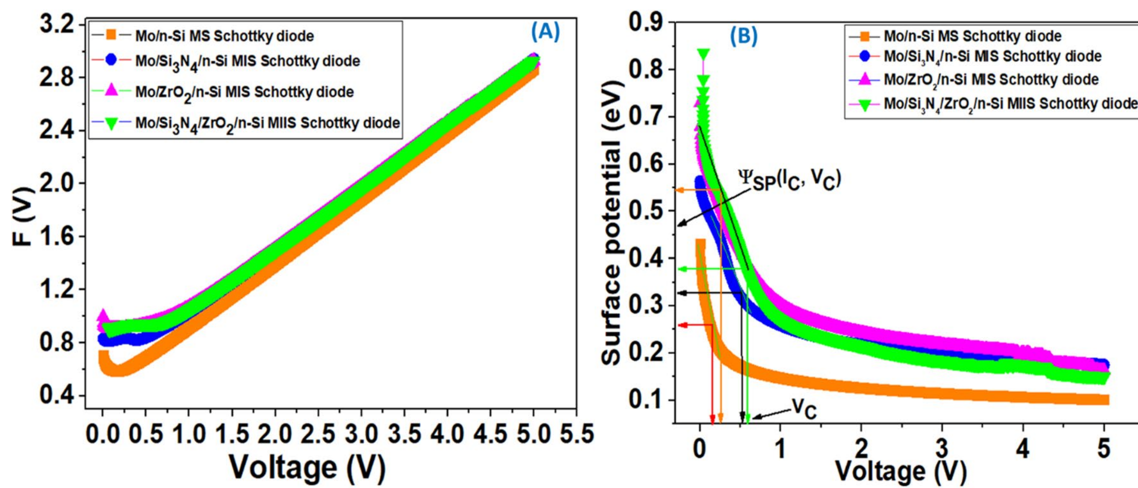

Fig. 9 **a** F(V)–V, **b** Ψ_{SP}–V plots for the Mo/n-Si (MS) SD, Mo/Si_3N_4/n-Si, Mo/ZrO_2/n-Si(MIS), Mo/Si_3N_4/ZrO_2/n-Si (MIIS) (single layer and double layer) SDs obtained from forward I–V characteristics

values. Therefore, the methods used in this study produce accurate and effective results. Table 3 summarizes the electrical properties of the MS SDand the MIS and MIIS SDs. The BH value of the double interlayer MIIS SDincreased compared to the single layer MIS SD, as shown in Table 3. This is because Zr, N, and O react with Si, resulting in the development of interfacial Zr–O–N and Zr-Si phases at the interface (as shown using XRD Fig. 3, XPS Fig. 4, and EDX Fig. 5). This is due to the changes in non-stoichiometric impurities near the interface, which increased BH. Another factor is that the development of these phases may induce vacant states in n-Si at the interface, which behave as deep acceptor states, causing an increase in BH when a double interlayer on the Si substrate. All Schottky barrier characteristics derived from Figs 7, 8, 9 using different methods were compared to the values in previous literature [29, 35, 41, 60, 63–65] and are listed in Table 3.

3.2.5 Forward bias (FB) current transport mechanism

A log (I)–log (V) plot is shown in Fig. 10a to identify the current conduction/transport mechanism in the entire FB region of the Mo/n-Si (MS) SD and Mo/Si_3N_4/n-Si, Mo/ZrO_2/n-Si (MIS), and Mo/Si_3N_4/ZrO_2/n-Si (MIIS) (single layer and double interlayer) SDs. The log (I)–log (V) plot for both diodes at different linear regions (region I, II, and III) with typical power exponents of formula $I \alpha V^m$ and the slope of the linear fit to the conduction mechanism plot can be used to calculate the exponential value m in this case. The results for regions I, II, and III are presented in Table 4. The values in a region I are close to unity, indicating that the current follows a linear relationship with I–V. This indicates that at low voltages, the current transmission affects Ohm's law, with background doping and thermally evolved carriers predominating over the injected charge carriers [8, 68]. The current gradually increases in the intermediate stage (region II). In region II, slope values greater than 2 indicate that the space-charge-limited current (SCLC) may dominate the current transport mechanism. However, the voltage in this region becomes more prominent than in region I, and the injected free charge carrier density is significantly higher than the thermally generated free charge carrier density [56]. The slope values tend to increase when the diode approaches the trap-filled limit current, whereas the injection level is high, with the same dependence as the trap-free SCLC [16].

3.2.6 Reverse bias current conduction mechanism

As shown in Fig. 10b, the reverse bias leakage current (I_R) of the MS SD, MIS, and MIIS SDs has an exponential relationship with the reverse bias voltage (V_R), indicating that the Poole–Frenkel emission (PFE) and Schottky emission (SE) mechanisms were active in the diodes. That is, regardless of the 2D-insulating layer, the ln (I_R)–$V_R^{1/2}$ plot (Fig. 10b) shows a linear change, implying that the reverse current will occur by the PFE or SE for all diodes. The reverse current owing to the PFE is described using the following equation [16, 61, 68].

$$I_R = I_o exp\left(\frac{\beta_{PF}\sqrt{V}}{K_B T\sqrt{d}}\right) \tag{6}$$

The current is determined by SE, and it may be calculated using

Table 3 Parameters determined from the forward and reverse bias I–V characteristics of the MS, MIS SDs, and MIIS SDin the present work, and comparison with the previously reported MIS Schottky and heterostructures in the literature

Parameters	Mo/n-Si	$Mo/Si_3N_4/n-Si$	$Mo/ZrO_2/n-Si$	$Mo/Si_3N_4/ZrO_2/n-Si$
BH (eV) from I–V	0.71	0.88	0.99	1.04
Ideality factor (n) from I–V	1.23	1.65	1.31	1.75
Leakage current at − 1 V	6.57E−6	1.83E−7	1.21E−8	1.95E−9
Ideality factor (n) from dV/d(lnI)	1.16	1.75	1.65	1.28
R_S (Ω) from dV/d(lnI)	64	3946	7711	3602
BH (eV) from H(I)	0.72	0.82	1.00	1.12
R_S (Ω) from H(I)	63	4193	7271	2675
BH (eV) from F(V)	0.73	0.89	1.02	1.16
R_S from F(V)	94 Ω	159 kΩ	2096 kΩ	53 MΩ
BH (eV) from Ψ_{SP}	0.71	0.92	0.91	0.98
Ideality factor (n) from Ψ_{SP}	1.19	1.81	1.57	1.45

Ref. no	From I–V plot		Cheung's functions				Norde method		Ψ_{SP}–V plot	
			dV/d(lnI)–I		H(I)–I					
	BH (eV)	n	R_S (Ω)	n	BH	R_S(Ω)	BH	R_S (Ω)	BH	n
Comparison with the literature										
[29]	0.95	2.1	–	–	–	–	–	–	–	–
[35]	0.74	1.37	334	–	–	301	0.73	–	–	–
[41]	1.04	2.64	238	–	–	–	–	–	–	–
[60]	1.12	3.77	4.412 k	3.56	1.10	3.95 k	–	–	–	
[65]	0.71	1.22	1.58 k	1.31	0.30	1.41 k	0.75	–	0.71	1.22
[67]	0.81	3.15	990	3.14	0.80	908	0.93	732	–	–
[68]	0.87	1.29	22.6 k	1.30	0.88	19.7 k	0.85	96.2 k	0.89	1.32
[63]	0.77	2.39	0.08	11.32	0.59	0.06	0.80	6.94		
[64]	0.68	6.5	9.37	–	–	56.47	–	–	–	–

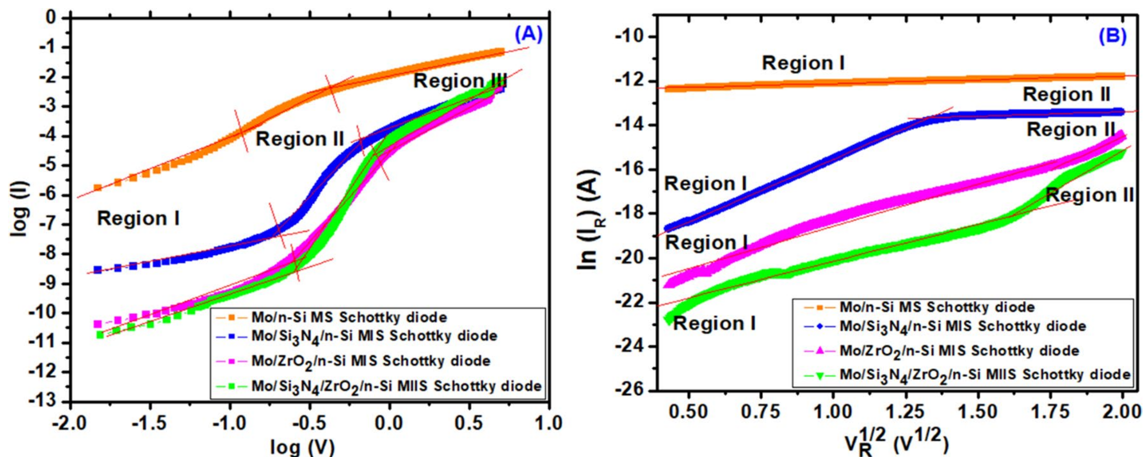

Fig. 10 **a** FB log(I)–log(V), **b** ln (I_R)–$V^{1/2}$ plots for the Mo/n-Si (MS) SD, $Mo/Si_3N_4/n-Si$, $Mo/ZrO_2/n-Si$(MIS), $Mo/Si_3N_4/ZrO_2/n-Si$ (MIIS) (single layer and double layer) SDs

Table 4 Forward conduction mechanism results of the MS SD, MIS, and MIIS SDs

Structure	Region-I	Region-II	Region-III
Mo/n-Si MS Schottky diode	1.99	2.74	1.13
Mo/Si_3N_4/n-Si MIS Schottky diode	1.13	7.08	2.09
Mo/ZrO_2/n-Si MIS Schottky diode	1.69	6.37	2.94
Mo/Si_3N_4/ZrO_2/n-Si MIIS Schottky diode	1.96	8.49	2.75

$$IR = AA^*T^2 exp\left(\frac{-\Phi_b}{kT}\right)exp\left(\frac{\beta_{SE}\sqrt{V}}{k_BT\sqrt{d}}\right) \quad (7)$$

where β_{PFE} and β_{SE} are the field-lowering coefficients of PFE and SE, respectively. The theoretical β_{PF} and β_{SE} values are as follows:

$$2\beta_{SE} = \beta_{PF} = \sqrt{\left(\frac{q^3}{\pi\varepsilon_o\varepsilon_r}\right)} \quad (8)$$

β_{PF} is always twice the value of β_{SE} in most cases. The theoretical field-lowering coefficients for the MS diode are $\beta_{PF} = 2.209 \times 10^{-5}$ eV $m^{1/2}$ $V^{-1/2}$ and $\beta_{SE} = 1.10 \times 10^{-5}$ eV $m^{1/2}$ $V^{-1/2}$, whereas the theoretical values of the MIS SD are $\beta_{PF} = 9.53 \times 10^{-5}$ eV $m^{1/2}$ $V^{-1/2}$ and $\beta_{SE} = 4.77 \times 10^{-5}$ eV $m^{1/2}$ $V^{-1/2}$. The experimental and equivalent values were extracted from the slope of the linear fitting of the ln (I_R)–$V_R^{1/2}$ plot. The calculated values for the Mo/n-Si SD is 1.99×10^{-5} eV $m^{1/2}$ $V^{-1/2}$ which is closely matched to the theoretical values of SE. It is therefore hypothesized that SE is the predominant charge conduction mechanism for the Mo/n-Si SD. Two distinct linear regions are readily seen in the plots of ln (I_R)–$V_R^{1/2}$ for the MIS and MIIS SDs (I and II; Fig. 10b). The experimentally determined slope values for the Mo/Si_3N_4/n-Si, Mo/ZrO_2/n-Si, and Mo/Si_3N_4/ZrO_2/n-Si SDs were 6.6×10^{-5} and 1.87×10^{-5}, 5.25×10^{-5} and 2.21×10^{-5}, and 7.26×10^{-5} and 2.55×10^{-5} eV $m^{1/2}$ $V^{-1/2}$, respectively. In the plots for the MIS and MIIS SDs, region I slope values (lower bias) were near to the theoretical values of β_{PF}, while region II slope values (higher bias) were close to the theoretical values of β_{SE}. This research shows that at lower biases the PFE mechanism controls reverse current conduction, while at higher biases SE is in control. SE involves current conduction via the contact interface as opposed to the bulk material because of the non-uniformity and native oxides of the insulating layers (Si_3N_4, ZrO_2 and Si_3N_4/ZrO_2). In the PF conduction mechanism, there is a wide distribution of traps in the insulating layer's bandgap that are caused by deficiencies or residues in the combination of the material. This might be the cause of the improved charge carrier trapping or detrapping performance [62, 63].

3.2.7 Energy band diagram

We suggest a mechanism for BH control for the Mo/n-Si (MS) SD, Mo/Si_3N_4/n-Si, Mo/ZrO_2/n-Si (MIS), and Mo/Si_3N_4/ZrO_2/n-Si (MIIS) (single layer and double interlayer) SDs using the BH values calculated from I–V, Norde's, Cheung's, and Chattopadhyay's methods. Figure 11 shows a reliable energy band diagram of the MS SDand the MIS SD.

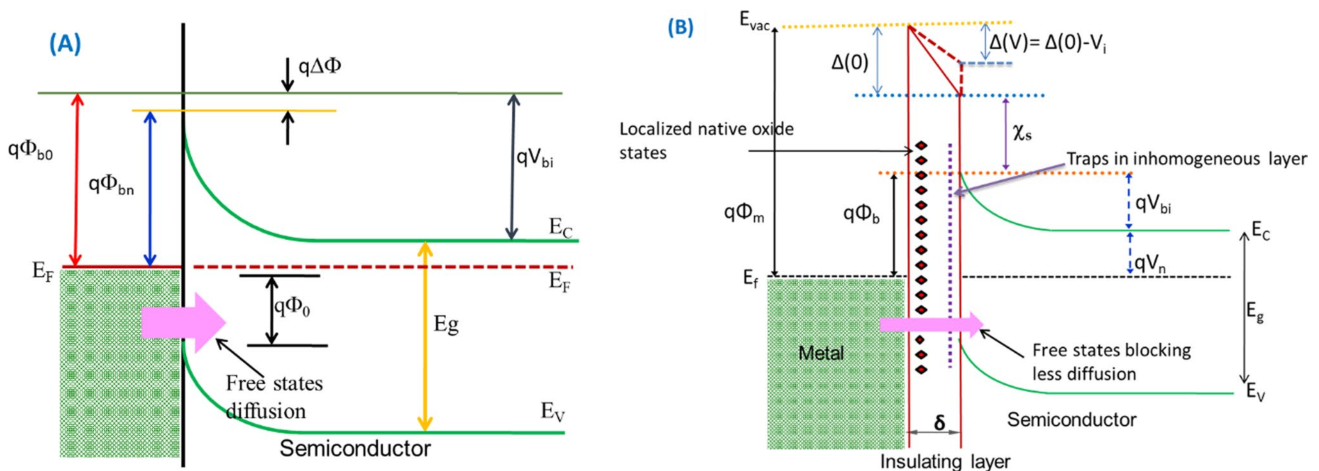

Fig. 11 Possible energy level band diagrams of the **a** MS SD and **b** Mo/insulating layer/n-Si SDs with free states, χ_S is electron affinity of semiconductor, E_g is energy band gap, ϕ_b is barrier height, ϕ_m is a metal work function, E_F is Fermi energy level, E_V is valence and E_C is CBs

Metal-induced gap states (MIGS) have pinned Fermi values at metal-semiconductor (SC) SDs [8, 16]. When a metal wave function decays into the SC and crates the MIGS, it results in the pinning of Fermi levels at the device interface [37, 64]. This could explain the permeation of free states into the metal electrode at contact (Fig. 11a). By restricting the metal wave function entry into the SC bandgap and doping the free states, an insulating layer can decrease the Fermi level pinning generated by the MIGS. Si_3N_4 and ZrO_2 acted as interlayers in this study (Fig. 11b), restricting free states at the actual MIS interface. Consequently, the effective BH values of the MIS and MIIS SDs increased.

4 Conclusion

High-quality wide bandgap and high-k Si_3N_4 and ZrO_2 films were effectively deposited on n-Si using thermal evaporation, DC, and RF-magnetron sputtering systems. Their optical, structural, morphological, and chemical properties were studied. The entire UV/Vis region of the electromagnetic spectrum was responsive. XRD results showed high-intensity refractions of the $ZrSiO_4$ (2 0 0), Zr_2ON_2 (4 0 0), $Zr_7O_{11}N_2$ (1 2 8), and $ZrSi_2$ (1 7 1) planes. XPS results indicated that the Si 2p spectrum centered at 101.7 eV was assigned to Si–N bonds, Zr $3d_{5/2}$, and Zr $3d_{3/2}$ peaks at 183.36 eV and 185.67, and O 1 s at 530.6 eV were attributed to the Zr–O bond in ZrO_2, and the presence of Si, Zr, N, and O were observed. The SEM images showed that the films were uniform, densely packed, and accurate on the surface, and EDX spectra confirmed the existence of Zr, Si, N, and O. AFM analysis showed that the overall surface morphology of all the films on n-Si was smooth. UV–VIS, XRD, XPS, SEM–EDX, and AFM investigations confirmed that Si_3N_4 and ZrO_2 films were formed on the n-Si substrate. Subsequently, Mo/Si_3N_4/n-Si, Mo/ZrO_2/n-Si (MIS), and Mo/Si3N4/ZrO_2/n-Si (MIIS) (single layer and double interlayer) SDs were fabricated, and their electrical properties were characterized through forward and reverse biased current–voltage (I–V) measurements at ambient temperature. The electrical characteristics were compared to those of a standard Mo/n-Si (MS) SD. Compared with the MS SD, the MIS SDexhibited good rectification properties and low reverse current leakage. The BH values estimated in MIIS SDwere higher than in MIS SDs and MS diode. In addition, Cheung's, Norde's, and Chattopadhyay's methods were used to compare the calculated BH, n, and R_S values of the MS, MIS SDs and MIIS SD. Energy-level band diagrams were used to describe the BH modulation method. According to the FB I–V characteristics, the MS, MIS, and MIIS diodes were ohmic in the lower bias region and SCLC in the high-voltage region. The reverse leakage current in the MS diode is therefore hypothesized that SE is the predominant charge conduction mechanism. The MIS and MIIS SDs shows two regions (lower and higher), in lower biases the PFE is the dominant reverse current conduction, while at higher biases SE is in dominant current conduction mechanism. Furthermore, Si_3N_4 and ZrO_2 are appropriate insulating layer materials for innovative optoelectronic device applications.

Supplementary Information The online version contains supplementary material available at https://doi.org/10.1007/s00339-023-06664-4.

Acknowledgements This work was supported by the National Research Foundation of Korea (NRF) grant funded by the Korea government (MSIT) (No. 2019R1A2C1089080).

Data availability statement The authors declare that the data supporting the findings of this study are available within the paper and its Supplementary Information files. Should any raw data files be needed in another format they are available from the corresponding author upon reasonable request.

References

1. P. Vivek, J. Chandrasekaran, R. Marnadu, S. Maruthamuthu, V. Balasubramani, P. Balraju, Zirconia modified nanostructured MoO_3 thin films deposited by spray pyrolysis technique for Cu/MoO_3-ZrO_2/p-Si structured Schottky barrier diode application. Optik **199**, 163351 (2019)
2. H.K. Khanfar, A.F. Qasrawi, Y.A. Zakarneh, N.M. Gasanly, Design and applications of YB/GA_2SE_3/C Schottky barrier. IEEE Sens. J. **17**, 4429–4434 (2017)
3. S. Riazimehr, S. Kataria, R. Bornemann, P. Haring Bolívar, F.J.G. Ruiz, O. Engström, A. Godoy, M.C. Lemme, High photocurrent in gated graphene-silicon hybrid photodiodes. ACS Photonics **4**, 1506–1514 (2017)
4. A. Di Bartolomeo, F. Giubileo, A. Grillo, G. Luongo, L. Iemmo, F. Urban, L. Lozzi, D. Capista, M. Nardone, M. Passacantando, Bias tunable photocurrent in metal-insulator-semiconductor heterostructures with photoresponse enhanced by carbon nanotubes. Nanomaterials (Basel) **9**, 1598 (2019)
5. M. Balaji, J. Chandrasekaran, M. Raja, R. Marnadu, M. Ramamurthy, M. Shkir, Fabrication of ON/OFF switching response based on n-Ni-doped MoO_3/p-Si junction diodes using Ni-MoO_3 thin films as n-type layer prepared by JNS pyrolysis technique. Appl. Phys. A **126**, 216 (2020)
6. M. Casalino, U. Sassi, I. Goykhman, A. Eiden, E. Lidorikis, S. Milana, D. De Fazio, F. Tomarchio, M. Iodice, G. Coppola, A.C. Ferrari, Vertically illuminated, resonant cavity enhanced, graphene-silicon Schottky photodetectors. ACS Nano **11**, 10955–10963 (2017)
7. L. Qian, Y. Sun, M. Wu, D. Xie, L. Ding, G. Shi, A solution-processed high-performance phototransistor based on a perovskite composite with chemically modified graphenes. Adv. Mater. **29**, 1606175 (2017)
8. V. Manjunath, V. Rajagopal Reddy, P.R. Sekhar Reddy, V. Janardhanam, C.-J. Choi, Electrical and frequency-dependent properties of Au/Sm_2O_3/n-GaN MIS junction with a high-k rare-earth Sm_2O_3 as interlayer. Curr. Appl. Phys. **17**, 980–988 (2017)
9. A. Ashery, M.M.M. Elnasharty, Dielectric assessment of epitaxially grown Al/SiO_2/Si heterojunction. SILICON **11**, 1875–1883 (2019)

10. Y. Liu, J. Yu, P.T. Lai, Investigation of WO_3/ZnO thin-film heterojunction-based Schottky diodes for H_2 gas sensing. Int. J. Hydrogen Energy **39**, 10313–10319 (2014)
11. H. Altuntas, A. Bengi, T. Asar, U. Aydemir, B. Sarıkavak, Y. Ozen, Ş Altındal, S. Ozcelik, Interface state density analyzing of Au/TiO_2(rutile)/n–Si Schottky barrier diode. Surf. Interface Anal. **42**, 1257–1260 (2010)
12. A. Turut, D.E. Yıldız, A. Karabulut, İ Orak, Electrical characteristics of atomic layer deposited Au/Ti/HfO_2/n-GaAs MIS diodes in the wide temperature range. J. Mater. Sci. Mater. Electron. **31**, 7839–7849 (2020)
13. H.G. Çetinkaya, D.E. Yıldız, Ş Altındal, On the negative capacitance behavior in the forward bias of Au/n–4H–SiC (MS) and comparison between MS and Au/TiO_2/n–4H–SiC (MIS) type diodes both in dark and under 200 W illumination intensity. Int. J. Mod. Phys. B **29**, 1450237 (2014)
14. D.E. Yıldız, A. Karabulut, İ Orak, A. Turut, Effect of atomic-layer-deposited HfO_2 thin-film interfacial layer on the electrical properties of Au/Ti/n-GaAs Schottky diode. J. Mater. Sci. Mater. Electron. **32**, 10209–10223 (2021)
15. A. Konar, D. Jena, Tailoring the carrier mobility of semiconductor nanowires by remote dielectrics. J. Appl. Phys. **102**, 123705 (2007)
16. J. Weng, S.-P. Gao, Structures and characteristics of atomically thin ZrO_2 from monolayer to bilayer and two-dimensional ZrO_2–MoS_2 heterojunction. RSC Adv. **9**, 32984–32994 (2019)
17. T. Tunç, İ Uslu, Fabrication and characterization of boron-doped yttria-stabilized zirconia nanofibers. Polym. Eng. Sci. **53**, 963–969 (2013)
18. S. Zhou, Z. Fang, H. Ning, W. Cai, Z. Zhu, J. Wei, X. Lu, W. Yuan, R. Yao, J. Peng, Bias stability enhancement in thin-film transistor with a solution-processed ZrO_2 dielectric as gate insulator. Appl. Sci. **8**, 806 (2018)
19. G. Koo, W. Lee, B. Kil, H. Ahn, B.W. Cho, S.H. Han, Enhancement of photoconversion efficiency of ZnO nanorod-based dye-sensitized solar cells in presence of ZrO_2 thin energy barrier. J. Nanosci. Nanotechnol. **11**, 4476–4479 (2011)
20. G.Q. Liu, H.T. Kuo, R.S. Liu, C.H. Shen, D.S. Shy, X.K. Xing, J.M. Chen, Study of electrochemical properties of coating ZrO_2 on $LiCoO_2$. J. Alloy. Compd. **496**, 512–516 (2010)
21. S. Kumar, A.K. Ojha, Oxygen vacancy induced photoluminescence properties and enhanced photocatalytic activity of ferromagnetic ZrO_2 nanostructures on methylene blue dye under ultraviolet radiation. J. Alloy. Compd. **644**, 654–662 (2015)
22. J.Y. Koo, Y. Lim, Y.B. Kim, D. Byun, W. Lee, Electrospun yttria-stabilized zirconia nanofibers for low-temperature solid oxide fuel cells. Int. J. Hydrogen Energy **42**, 15903–15907 (2017)
23. A.S. Mokrushin, E.P. Simonenko, N.P. Simonenko, K.A. Bukunov, V.G. Sevastyanov, N.T. Kuznetsov, Gas-sensing properties of nanostructured CeO_2-ZrO_2 thin films obtained by the sol-gel method. J. Alloy. Compd. **773**, 1023–1032 (2019)
24. K.S. Mohan, A. Panneerselvam, J. Chandrasekaran, R. Marnadu, M. Shakir, An in-depth examination of optoelectrical properties of In-Yb_2O_3 thin films and fabricated Al/In-Yb_2O_3/p-Si (MIS) heterojunction diodes. Appl. Nanosci. **11**, 1617–1635 (2021)
25. R. Ramaseshan, S. Sundarrajan, R. Jose, S. Ramakrishna, Nanostructured ceramics by electrospinning (2007)
26. O. Saligheh, R. Khajavi, M.E. Yazdanshenas, A. Rashidi, Production and characterization of zirconia (ZrO_2) ceramic nanofibers by using electrospun poly(vinyl alcohol)/zirconium acetate nanofibers as a precursor. J. Macromol. Sci. Part B **55**, 605–616 (2016)
27. S.M. Razavi, S. Tahmasb Pour, P. Najari, New GaN based HEMT with Si_3N_4 or un-doped region in the barrier for high power applications. Superlattices Microstruct. **118**, 221–229 (2018)
28. Z. Zhang, G. Yu, X. Zhang, S. Tan, D. Wu, K. Fu, W. Huang, Y. Cai, B. Zhang, 16.8 A/600 V AlGaN/GaN MIS-HEMTs employing LPCVD-Si_3N_4 as gate insulator. Electron. Lett. **51**, 1201–1203 (2015)
29. D.A. Zakheim, W.V. Lundin, A.V. Sakharov, E.E. Zavarin, P.N. Brunkov, E.Y. Lundina, A.F. Tsatsulnikov, S.Y. Karpov, Dependence of leakage current in Ni/Si_3N_4/n-GaN Schottky diodes on deposition conditions of silicon nitride. Semicond. Sci. Technol. **33**, 115008 (2018)
30. E. Kim, N. Soejima, Y. Watanabe, M. Ishiko, T. Kachi, Electrical properties of metal-insulator-semiconductor capacitors on free-standing GaN substrate. Jpn. J. Appl. Phys. **49**, 04DF08 (2010)
31. J. Bauer, Optical properties, band gap, and surface roughness of Si_3N_4. Phys. Status Solidi (a) **39**, 411–418 (1977)
32. S. Tongay, W. Fan, J. Kang, J. Park, U. Koldemir, J. Suh, D.S. Narang, K. Liu, J. Ji, J. Li, R. Sinclair, J. Wu, Tuning interlayer coupling in large-area heterostructures with CVD-grown MoS_2 and WS_2 monolayers. Nano Lett. **14**, 3185–3190 (2014)
33. F. Schwierz, J. Pezoldt, R. Granzner, Two-dimensional materials and their prospects in transistor electronics. Nanoscale **7**, 8261–8283 (2015)
34. H.-C. Liu, X.-G. Tang, Q.-X. Liu, Y.-P. Jiang, W.-H. Li, X.-B. Guo, Z.-H. Tang, Bipolar resistive switching behavior and conduction mechanisms of composite nanostructured TiO_2/ZrO_2 thin film. Ceram. Int. **46**, 21196–21201 (2020)
35. R. Coloma Ribera, R.W.E. van de Kruijs, J.M. Sturm, A.E. Yakshin, F. Bijkerk, Intermixing and thermal oxidation of ZrO_2 thin films grown on a-Si, SiN, and SiO_2 by metallic and oxidic mode magnetron sputtering. J. Appl. Phys. **121**, 115303 (2017)
36. H.C. Barshilia, B. Deepthi, K.S. Rajam, Stabilization of tetragonal and cubic phases of ZrO_2 in pulsed sputter deposited ZrO_2/Al_2O_3 and ZrO_2/Y_2O_3 nanolayered thin films. J. Appl. Phys. **104**, 113532 (2008)
37. Ş Altındal, Y. Azizian-Kalandaragh, M. Ulusoy, G. Pirgholi-Givi, The illumination effects on the current conduction mechanisms of the Au/(Er_2O_3:PVC)/n-Si (MPS) Schottky diodes. J. Appl. Polym. Sci. **139**, e52497 (2022)
38. S. Chopra, R.P. Gupta, S. Banerjee, Hydrogen dependent surface morphology study of plasma deposited SiNx:H films for two gas systems SiH_4/NH_3 and SiH_4/N_2, in 2010 3rd International Nanoelectronics Conference (INEC), pp. 376–377 (2010)
39. H. Kaji, H. Kondo, T. Fujii, M. Arita, Y. Takahashi, Effect of electrode and interface oxide on the property of ReRAM composed of $Pr_{0.7}Ca_{0.3}MnO_3$. IOP Conf. Ser. Mater. Sci. Eng. **8**, 012032 (2010)
40. N. Nanda Kumar Reddy, S. Godavarthi, K. Mohan Kumar, V.K. Kummara, S.V. Prabhakar Vattikuti, H.S. Akkera, Y. Bitla, S.A.K. Jilani, V. Manjunath, Evaluation of temperature-dependent electrical transport parameters in Fe_3O_4/SiO_2/n-Si metal-insulator-semiconductor (MIS) type Schottky barrier heterojunction in a wide temperature range. J. Mater. Sci. Mater. Electron. **30**, 8955–8966 (2019)
41. S. Adachi, H. Wakana, M. Horibe, N. Inoue, T. Sugano, K. Tanabe, Preparation of La-doped Yb-123 thin films for high-Tc devices. Phys. C Supercond. **378–381**, 1213–1215 (2002)
42. R. Marnadu, J. Chandrasekaran, S. Maruthamuthu, P. Vivek, V. Balasubramani, P. Balraju, Jet nebulizer sprayed WO_3-nanoplate arrays for high-photoresponsivity based metal-insulator-semiconductor structured Schottky barrier diodes. J. Inorg. Organomet. Polym Mater. **30**, 731–748 (2020)
43. S. Phokha, S. Pinitsoontorn, P. Chirawatkul, Y. Poo-arporn, S. Maensiri, Synthesis, characterization, and magnetic properties of monodisperse CeO_2 nanospheres prepared by PVP-assisted hydrothermal method. Nanoscale Res. Lett. **7**, 425 (2012)
44. A.V. Prokofiev, A.I. Shelykh, B.T. Melekh, Periodicity in the band gap variation of Ln_2X_3 (X = O, S, Se) in the lanthanide series. J. Alloy. Compd. **242**, 41–44 (1996)

45. K. Sasikumar, R. Bharathikannan, M. Raja, B. Mohanbabu, Fabrication and characterization of rare earth (Ce, Gd, and Y) doped ZrO_2 based metal-insulator-semiconductor (MIS) type Schottky barrier diodes. Superlattices Microstruct. **139**, 106424 (2020)
46. A. Büyükbaş-Uluşan, A. Tataroğlu, Impedance spectroscopy of Au/TiO_2/n-Si metal-insulator-semiconductor (MIS) capacitor. Phys. B **580**, 411945 (2020)
47. M. Waghmare, P. Sonone, P. Patil, V. Kadam, H. Pathan, A. Ubale, Spray pyrolytic deposition of zirconium oxide thin films: influence of concentration on structural and optical properties. Eng. Sci. **5**, 79–87 (2019)
48. B.-H. Liao, C.-N. Hsiao, M.-H. Shiao, S.-H. Chen, Characterization of silicon oxynitride films deposited by a high-power impulse magnetron sputtering deposition technique. Appl. Opt. **59**, A176–A180 (2020)
49. Z.Q. Yao, P. Yang, N. Huang, H. Sun, G.J. Wan, Y.X. Leng, J. Wang, J.Y. Chen, Fabrication and surface characterization of pulsed reactive closed-field unbalanced magnetron sputtered amorphous silicon nitride films. Surf. Coat. Technol. **200**, 4144–4151 (2006)
50. X. Yin, X. Xie, L. Song, Y. Zhou, P. Du, J. Xiong, The application of highly flexible ZrO_2/C nanofiber films to flexible dye-sensitized solar cells. J. Mater. Sci. **52**, 11025–11035 (2017)
51. V.V. Kondalkara, X. Lia, S. Yanga, K. Leea, Current sensor based on nanocrystalline NiFe/Cu/NiFe thin film. Proc. Eng. **168**, 675–679 (2016)
52. H. Zhang, H. Ding, M. Wei, C. Li, B. Wei, J. Zhang, Thin film encapsulation for organic light-emitting diodes using inorganic/organic hybrid layers by atomic layer deposition. Nanoscale Res. Lett. **10**, 169 (2015)
53. E.H.W.R.H. Rhoderick, Metal-semiconductor contacts (Clarendon Press, Oxford University Press, Oxford, 1988)
54. D. Tomer, S. Rajput, L.J. Hudy, C.H. Li, L. Li, Inhomogeneity in barrier height at graphene/Si (GaAs) Schottky junctions. Nanotechnology **26**, 215702 (2015)
55. Z. Çaldıran, Modification of Schottky barrier height using an inorganic compound interface layer for various contact metals in the metal/p-Si device structure. J. Alloy. Compd. **865**, 158856 (2021)
56. V. Rajagopal Reddy, V. Manjunath, V. Janardhanam, Y.-H. Kil, C.-J. Choi, Electrical properties and current transport mechanisms of the Au/n-GaN Schottky structure with solution-processed high-k $BaTiO_3$ interlayer. J. Electron. Mater. **43**, 3499–3507 (2014)
57. K. Sasikumar, R. Bharathikannan, M. Raja, Effect of annealing temperature on structural and electrical properties of Al/ZrO_2/p-Si MIS Schottky diodes. SILICON **11**, 137–143 (2019)
58. H. Norde, A modified forward I–V plot for Schottky diodes with high series resistance. J. Appl. Phys. **50**, 5052–5053 (1979)
59. P. Chattopadhyay, A new technique for the determination of barrier height of Schottky barrier diodes. Solid State Electron. **38**, 739–741 (1995)
60. S. Chattopadhyay, L.K. Bera, S.K. Ray, P.K. Bose, C.K. Maiti, Extraction of interface state density of Pt/p-strained-Si Schottky diode. Thin Solid Films **335**, 142–145 (1998)
61. V. Manjunath, N.K.R. Nallabala, C. Yuvaraj, C. Kukkambakam, V.K. Kummara, S. Kumar, S. Sharma, M.V. Lakshmaiah, V.R. Minnam Reddy, Statistical analysis of current-voltage characteristics in Au/Ta_2O_5/n-GaN Schottky barrier heterojunction using different methods. Appl. Phys. A **127**, 46 (2021)
62. A. Tatarolu, Comparative study of electrical properties of Au/n-Si (MS) and Au/Si_3N_4/n-Si (MIS) Schottky diodes. Chin. Phys. B **22**, 68402–068402 (2013)
63. R. Padma, G. Lee, J.S. Kang, S.C. Jun, Structural, chemical, and electrical parameters of Au/MoS_2/n-GaAs metal/2D/3D hybrid heterojunction. J. Colloid Interface Sci. **550**, 48–56 (2019)
64. P. Harishsenthil, J. Chandrasekaran, R. Marnadu, P. Balraju, C. Mahendran, Influence of high dielectric HfO_2 thin films on the electrical properties of Al/HfO_2/n-Si (MIS) structured Schottky barrier diodes. Phys. B **594**, 412336 (2020)
65. S. Alialy, Ş Altındal, E.E. Tanrıkulu, D.E. Yıldız, Analysis of temperature dependent current-conduction mechanisms in Au/TiO_2/n-4H-SiC (metal/insulator/semiconductor) type Schottky barrier diodes. J. Appl. Phys. **116**, 083709 (2014)
66. S. Demirezen, S. AltındalYerişkin, A detailed comparative study on electrical and photovoltaic characteristics of Al/p-Si photodiodes with coumarin-doped PVA interfacial layer: the effect of doping concentration. Polym. Bull. **77**, 49–71 (2020)
67. S. Demirezen, H.G. Çetinkaya, Ş Altındal, Doping rate, interface states and polarization effects on dielectric properties, electric modulus, and AC conductivity in PCBM/NiO:ZnO/*p*-Si structures in wide frequency range. SILICON **14**, 8517–8527 (2022)
68. A. Eroğlu, S. Demirezen, Y.A. Kalandaragh, Ş Altındal, A comparative study on the electrical properties and conduction mechanisms of Au/*n*-Si Schottky diodes with/without an organic interlayer. J. Mater. Sci. Mater. Electron. **31**, 14466–14477 (2020)
69. Ç. Bilkan, S. Zeyrek, S.E. San, Ş Altındal, A compare of electrical characteristics in Al/p-Si (MS) and Al/$C_{20}H_{12}$/p-Si (MPS) type diodes using current–voltage (I–V) and capacitance–voltage (C–V) measurements. Mater. Sci. Semicond. Process. **32**, 137–144 (2015)

Publisher's Note Springer Nature remains neutral with regard to jurisdictional claims in published maps and institutional affiliations.

Springer Nature or its licensor (e.g. a society or other partner) holds exclusive rights to this article under a publishing agreement with the author(s) or other rightsholder(s); author self-archiving of the accepted manuscript version of this article is solely governed by the terms of such publishing agreement and applicable law.

Authors and Affiliations

V. Manjunath[1,2] · B. Purusottam Reddy[1] · U. Chalapathi[1] · Boseong Son[1] · Huijin Kim[1] · Chang-Hoi Ahn[1] · Si-Hyun Park[1]

✉ V. Manjunath
drvmanju18@gmail.com

✉ Si-Hyun Park
sihyun_park@ynu.ac.kr

B. Purusottam Reddy
purusottam.svu@gmail.com

[1] Department of Electronic Engineering, Yeungnam University, 280 Daehak-ro, Gyeongsan-si, Gyongsanbuk-do 38541, Republic of Korea

[2] Department of Physics, Sri Padmavati Mahila Viswavidyalayam, Tirupati, Andhra Pradesh, India